



From waste to raw chemicals: Catalytic transformation of fusel oil by mixed metal oxides

Livia Padilha de Lima^a, Jorge Andrés Mora Vargas^{b,c}, Antonio Carlos Roveda Jr.^{b,d},
Julieth Orduna Ortega^c, Felipe Garcia da Silva^a, Rafael Francisco Cassaro^a,
Daniel Rodrigues Cardoso^b, Mauricio Boscolo^a, Gustavo Metzker^{a,*}

^a Sao Paulo State University (UNESP), Department of Chemistry and Environmental Sciences (IBILCE), Sao Jose do Rio Preto, SP, Brazil

^b University of Sao Paulo (USP), Sao Carlos Institute of Chemistry (IQSC), Sao Carlos, Brazil

^c Universidad Santiago de Cali, Facultad de Ciencias Básicas, Campus Pampalinda, Santiago de Cali, Colombia

^d Sao Paulo State University (UNESP), Institute of Geosciences and Exact Sciences, Rio Claro, SP, Brazil

ARTICLE INFO

Keywords:

Fusel oil

Mixed metal oxides

Organic building blocks

ABSTRACT

In this study, we detail a catalytic process for the conversion of fusel oil (FO), a by-product of ethanol production considered as waste, into valuable organic compounds, including aldehydes, alkenes, ketones, and alkylbenzenes spanning a carbon chain length from C₆ to C₁₂. The reaction was carried out in a fixed bed flow reactor at atmospheric pressure, employing mixed metal oxides (MMO) derived from hydrotalcites (HTC) as catalysts. The HTC were readily synthesized by co-precipitation method involving Mg²⁺ and Al³⁺, wherein 20 mol% Mg²⁺ was substituted by M²⁺ = Mn, Fe, Co, Ni, Cu, and Zn, and MMO obtained by HTC calcination. These catalysts offer cost-effectiveness compared to noble metal-containing ones while exhibiting remarkable activity in dehydrogenation, hydrogenation, and dehydration reactions pivotal for alcohol reactivity. The proposed methodology holds promise for large-scale industrial use and pioneers a fresh avenue for deriving value-added raw chemicals from a renewable carbon source.

1. Introduction

The Brazilian sugarcane industry is responsible for producing 598 million tons of sugarcane and 31.4 billion L of ethanol in 2022–2023, one of the most critical economic branches in the country's economy [1, 2]. Although the sugarcane industry contributes to diminishing CO₂ emissions due to the use of ethanol instead of gasoline as fuel for internal combustion engines, sugarcane processing generates considerable amounts of by-products. For example, producing 1000 L of ethanol requires, *c.a.*, 12 tons of sugarcane and generates 3 tons of bagasse, 1.8 tons of straw, 18,000 L of vinasse, and 2.5 L of fusel oil (FO) as the main solid and liquid by-products [3–11]. The bagasse is currently burned to generate electrical energy, and it is the focus of research for its utilization for second-generation ethanol or to convert to phenolic compounds obtained from lignin [5,6]. The straw is used as fertilizer and is the focus of the same research on the bagasse [5,6]. The vinasse is employed as a nitrogen, phosphorous, and potassium (NPK) source and is irrigated in the soil as a partial NPK replacement for the new crop [7]. However, the

FO has not gained the same attention as the other sugarcane processing by-products.

The yeast produces FO during the sugar fermentation stage of ethanol production [12]. FO percentage composition varies according to the sugarcane species and yeast strain employed in the fermentation process, being approximately 80% of 3-methyl-1-butyl (isoamyl alcohol, IA), 9% of isobutyl, 3% of ethyl, 1% of propyl, and 0.5% of 1-butyl alcohols and 6.5% of other minor products [12,13]. Although each 1000 L of ethanol generates only 2.5 L of FO, putting in perspective the 2022–2023 ethanol production in Brazil, the generation of *c.a.* 78.5 million L of FO is expected. The United States, European Union, and China are also significant producers of FO, with world production estimated at *c.a.* 550 million L in 2019 [8]. Most of the FO is treated as waste and burned to produce heat, contributing to the increase in CO₂ emissions and losing its potential as a renewable carbon source [12].

Trying to change the perspective mentioned above, there are few studies in the literature on FO utilization as a gasoline blend [14,15], substrate for the esterification reaction of the IA into isoamyl acetate,

* Corresponding author.

E-mail address: g.metzker@unesp.br (G. Metzker).

<https://doi.org/10.1016/j.apcatb.2024.123985>

Received 14 September 2023; Received in revised form 22 February 2024; Accepted 18 March 2024

Available online 19 March 2024

0926-3373/© 2024 Elsevier B.V. All rights reserved.

which can be used as a flavoring agent and green solvent [16–20], substrate for H_2 production through steam reforming reaction [21,22] and the conversion into light-[23] and long-chain hydrocarbons and aromatics starting from a mixture of ethanol and FO using zeolite as catalyst [24].

The catalytic transformation of FO alcohols into their respective aldehydes via dehydrogenation is a novel and unexplored approach. In a subsequent step, aldehydes and alcohols can react via Aldol condensation in a Guerbet-type mechanism [25–28], lengthening the carbon chain to produce long-chain hydrocarbons. Furthermore, the alcohols can be dehydrated to produce alkenes, which are reactive species for additional chemical transformations. From this perspective, the FO may represent a renewable carbon source from C_2 to C_5 , allowing the sustainable synthesis of long-chain hydrocarbons. However, to achieve the abovementioned goals, the catalyst platform must perform multiple and simultaneous reactions such as de- and hydrogenation and dehydration reactions [29,30].

Our Research Group has been working with magnesium-aluminum-based mixed metal oxides (MMO) and first-row transition metal divalent cations that partially substitute Mg^{2+} as a catalyst platform to convert alcohols into high-added value products [25,26,31–35]. These MMO are noble metal-free, easy to synthesize, and very active in dehydrogenation, hydrogenation, condensation, and dehydration reactions [36,37]. The MMO is a versatile platform since it can fine-tune the catalyst activity by changing the divalent cation in its structure. These MMO were applied to the Guerbet reaction of ethanol (C_2), obtaining 1-butyl alcohol (C_4) in batch and fixed-bed flow reactors with high yields [25,38]. Subsequently, the catalytic transformation of 1-butyl alcohol into aldehydes, ketones, alkenes, and aromatic compounds was also achieved with the same catalysts [26]. Thus, thinking on the advance of the full utilization of the sugarcane industry by-products aiming to diminish the environmental impact and aggregate more value to this industrial chain, the transformation of FO alcohols into high-added value organic building blocks, employing mixed metal oxides as catalysts was studied.

2. Experimental section

2.1. Reagents

All the salts utilized in the syntheses were purchased from Sigma-Aldrich (United States and Germany) and utilized without further purification. For the synthesis procedures, deionized water was utilized. IA (anhydrous >99%) was purchased from Sigma-Aldrich and utilized as received. Methanol (ACS grade) for the catalytic reactions was purchased from Labsynth (Brazil), and for the gas chromatography coupled with mass spectrometer (GC-MS) analyses, it was purchased from Sigma-Aldrich (GC-MS grade). The FO samples, gently gifted from Santa Isabel Sugarcane Mill, Novo Horizonte, Sao Paulo State, Brazil, were homogenized and filtered to eliminate any solids. After the filtration, the water was removed by a separatory funnel, and the remaining water was removed by treating the FO with anhydrous $MgSO_4$ (100 g·L⁻¹ of FO) under stirring for 24 h. Then, the FO was filtered using quantitative filter paper (22 μ m) to remove any $MgSO_4$. The FO was kept under a molecular sieve (3 Å) before utilization.

2.2. Catalysts synthesis and characterization

The HTC, the catalysts precursors, with a $Mg^{2+}:Al^{3+}$ molar ratio of 3:1 were synthesized by the co-precipitation method, as described before [25,39,40]. For this study, 20 mol% of the theoretical magnesium initial content was substituted by the same amount of $M^{2+} = Mn, Fe, Co, Ni, Cu$, and Zn from their respective nitrate salts. The obtained materials were labeled $M_{20}HTC$, where M is the metallic ion that substituted the Mg^{2+} and 20 means the amount of the Mg^{2+} ion that was replaced. The MMO, employed as catalysts, were obtained by HTC calcination at 450

°C for 5 h before utilization. The MMO was labeled as $M_{20}MMO$, following the same guidelines as HTC.

The samples of HTC and MMO were characterized by powder X-ray diffraction (XRD) to confirm the obtainment of the materials by comparing the diffractogram fingerprints with previous ones reported in the literature. The HTC was also characterized by thermogravimetric analysis (TGA). A detailed description of the characterization methodology and equipment utilized is in the [Supplementary Material](#).

2.3. Catalytic assays and products identification and quantification by GC-MS

As described before, the catalytic reactions were carried out in a fixed-bed flow reactor operating at atmospheric pressure [25,26]. The $M_{20}MMO$ (0.17 g) was dispersed in silica (1.53 g), homogenized, and the reactor column packed. It is important to recall that silica did not promote significant conversion of FO or IA at the reaction temperatures. The $M_{20}MMO$ was activated before the IA and FO reactions by pumping methanol (flow of 0.1 mL·min⁻¹) at 550 °C for 30 min. Thus, the methanol was substituted by the working solutions of methanol:IA (30:70 v/v) or methanol:FO (30:70 v/v) with flow rates of 0.1- or 0.2 mL·min⁻¹ and reactor oven temperature at 500, 550, or 600 °C adjusted according to the experiment. The condensed products were collected in 30, 60, 120, 180, 240, 300, and 360 min of reaction in 10 mL vials. The vials were kept at -20 °C until prior to the analysis. The condensed phase products were identified and quantified by GC-MS following the sample preparation and analysis methodology described before [25,26] and detailed in [Supplementary Material](#).

2.4. Post-mortem catalyst characterization

After the reactions, the $M_{20}MMO$ was characterized by XRD, following the same experimental conditions utilized before the reactions. The $M_{20}MMO$ was also characterized by TGA, scanning electron microscopy (SEM), and Raman spectroscopy aiming to identify and quantify the carbon deposition over the catalyst. The samples preparation and the experimental conditions for each technique are detailed in the [Supplementary Material](#).

3. Results

3.1. Catalysts characterization

The $M_{20}HTC$ were characterized by XRD, whose diffractograms are depicted in [Fig. S1](#). The $M_{20}HTC$ presented the fingerprint expected for hydrotalcite-like materials (reference diffraction pattern JCPDS 22-0700) with seven diffraction peaks between 5 and 70° [41,42]. The exception was $Mn_{20}HTC$, which presented two extra peaks at $2\theta = 31.8$ and 52.4° attributed to the presence of $MnCO_3$ (reference diffraction pattern JCPDS 44-1472) in the structure [43,44].

The HTC were calcined at 450 °C for 5 h, giving rise to $M_{20}MMO$ with the expected three-peaks fingerprint between 30 and 65°, all characteristic of MgO periclase (reference diffraction pattern JCPDS 45-0946) as can be observed in [Fig. S2](#). Again, the exception was $Mn_{20}MMO$ which presented low-intensity extra peaks at 18.4, 33.1, 39.1, 51.9, 59.5, 61.7, and 75.5° attributed to Mn_3O_4 and/or $MgMn_2O_4$ with reference diffraction patterns JCPDS 80-0382 and JCPDS 23-0392, respectively [43,44]. Since both diffraction patterns are very similar, it is not possible to claim which structure is present in the sample.

HTC was also characterized by TGA analysis by heating the samples from 50 to 800 °C, as depicted in [Fig. S3](#). All $M_{20}HTC$ presented three thermal events, one *c.a.* 110 °C related to the desorption of water in the material surface and the other two thermal events, *c.a.* 215 and 410 °C related to water removal and carbonate decomposition in the intralamellar space, respectively [31,42]. Taking into account the last two thermal events, which are by far more intense than the first one, the

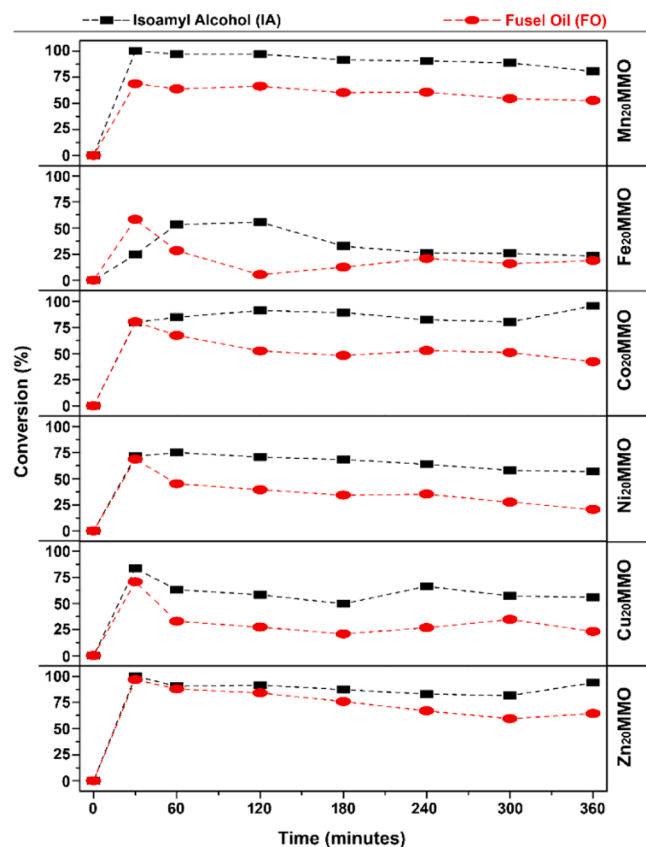


Fig. 1. Temporal behavior observed for IA (black) and FO (red) conversion for $M_{20}MMO$ catalysts. Conditions: 550 °C, reagent flow of 0.1 mL·min⁻¹, 30:70 of methanol: reagent (v/v) (IA or FO). For FO, the conversion means the sum of isoamyl, isobutyl, 1-butyl, and ethyl alcohols.

weight loss of the material corresponds to c.a. 37%, as can be observed in Table S1, which is in the same range of other hydrotalcite-like materials reported in the literature [32,42]. As expected, the $M_{20}MMO$ did not present any weight loss in the 50–800 °C temperature range.

3.2. Exploratory catalytic runs

The FO sample was evaluated prior to the initial assays for the choice of the catalytic conditions to determine its components and relative percentages of alcohols as follows: isoamyl (79.9), isobutyl (15.4), 1-butyl (3.2), and ethyl (1.5). There were no other organic volatile chemicals found.

The first catalytic assays were performed to define the best conditions for the FO transformation regarding temperature and flow. Since FO is a complex mixture of alcohols, our first attempt was to conduct the reaction only with IA, which is the major component of the FO mixture and was used as the reaction model compound. Considering our previous experience with MMO and alcohols catalytic transformations in fixed bed flow reactors, the temperature was set at 500, 550, and 600 °C and the FO flow at 0.1- and 0.2 mL·min⁻¹. After the first assays for all $M_{20}MMO$ (36 experiments), our best result was c.a. 40% IA conversion for $Zn_{20}MMO$ at 600 °C and 0.1 mL·min⁻¹. The low substrate conversion was also observed in previous studies in our Group for the catalytic reaction of 1-butyl alcohol by $Cu_{20}MMO$, and to improve it, the 1-butyl alcohol was mixed with methanol in the proportion of 70:30 (v/v) [26]. Thus, IA was mixed with 30% (v/v) of methanol, and the catalytic assays were repeated. The methanol addition enhances the catalyst's reactivity due to its reforming reaction, generating H_2 [26]. The IA conversion for all catalysts was higher than the ones observed for the reaction without methanol, and the better reaction conditions for all catalysts were a temperature of 550 °C and a flow of 0.1 mL·min⁻¹. At 500 °C, the conversion was lower in both flow conditions than those found for 550 and 600 °C. At 600 °C, almost no condensed product was observed in both flows, producing a large amount of gas, probably due to the reforming reaction as reported before for FO [21,22]. The same reaction conditions (30% methanol, 550 °C, and flow of 0.1 mL·min⁻¹)

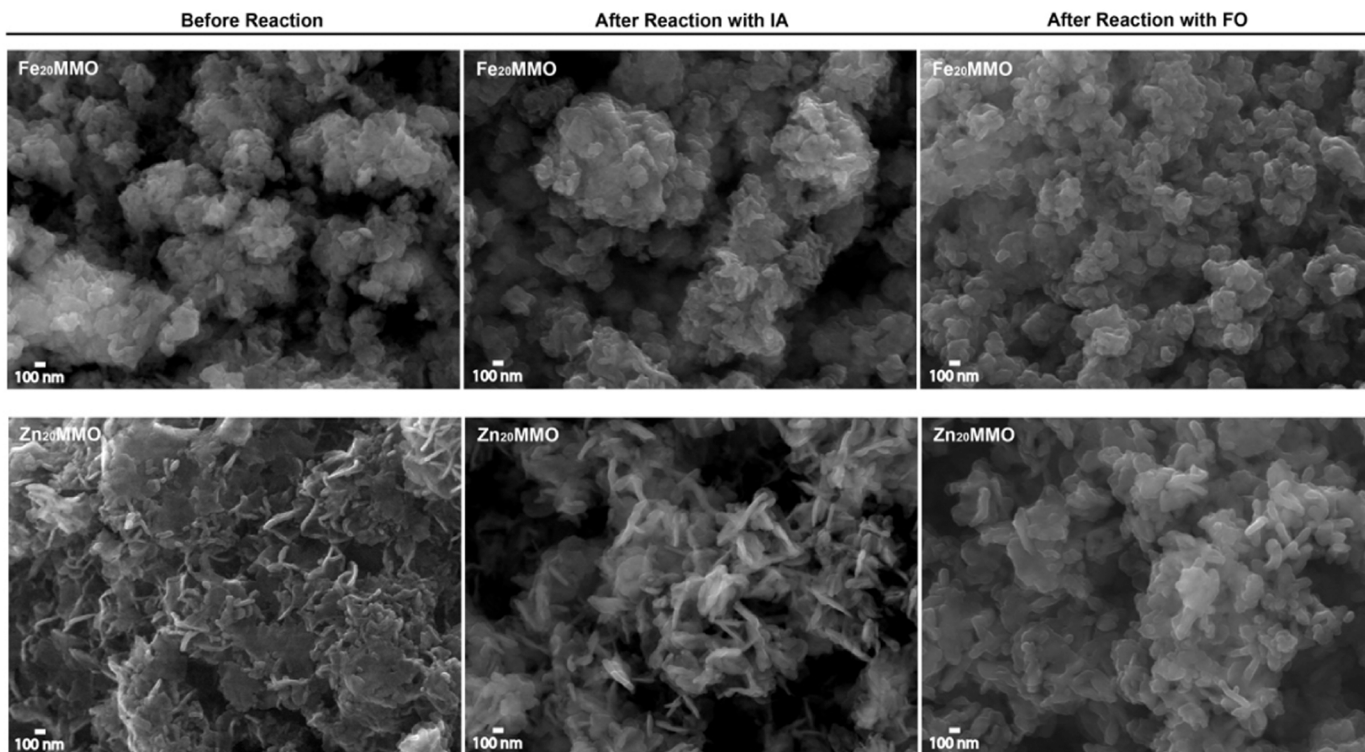


Fig. 2. SEM images of $Fe_{20}MMO$ and $Zn_{20}MMO$ before and after reactions with IA and FO.

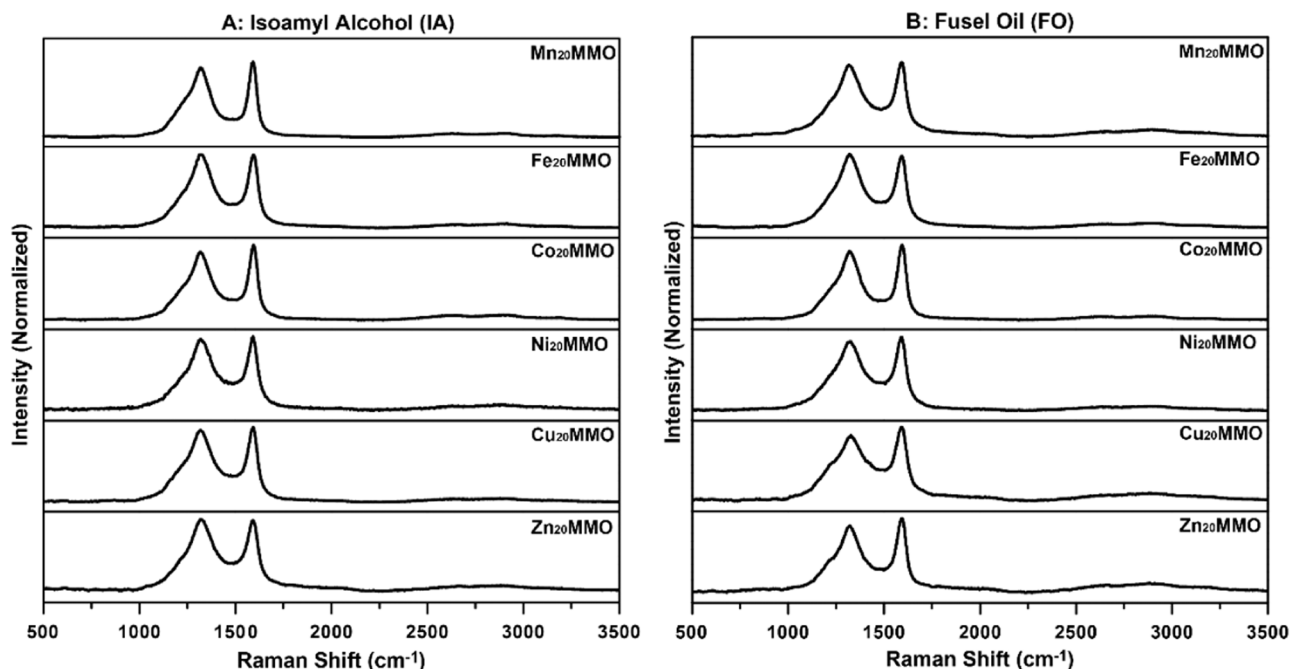


Fig. 3. Raman spectra of the M_{20} MMO catalysts after the reaction. A: IA; B: FO.

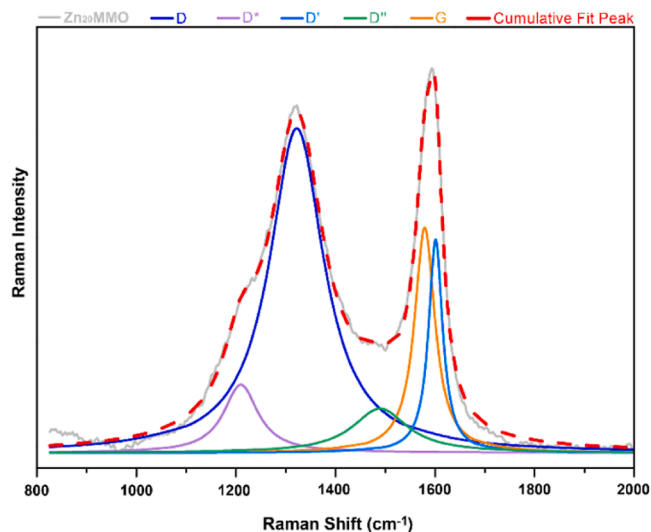


Fig. 4. Deconvolution of the first-order Raman spectrum of Zn_{20} MMO after reaction with FO.

were applied to FO and were also the best. Fig. 1 depicts the temporal behavior of the IA and FO conversions during the 6 h of reaction for all M_{20} MMO.

As can be observed in Fig. 1 and taking into account the temporal conversion behavior for IA and M_{20} MMO catalysts, it was observed that all M_{20} MMO presented decreasing conversion, except for $M^{2+} = Co$ and Zn , the ones that had a sudden increase at 300 min of reaction, with conversion nearing 90%. The Mn_{20} MMO also had satisfactory performance, although in a continuous conversion decrease, being c.a. 80% at 360 min. The Fe_{20} MMO presented the worst performance, with a significant initial conversion drop at 30 min, reaching 25% of conversion at 360 min.

Changing the IA for FO, all M_{20} MMO showed a significant drop in the conversion values (c.a. 20% compared with the IA) except for Fe_{20} MMO, which presented the same conversion value at 360 min. Also, the

Table 1

Carbon deposition, calculated by TGA, over M_{20} MMO surface after the reaction with IA and FO.

M_{20} MMO	Isoamyl Alcohol (IA)		Fusel Oil (FO)	
	Thermal Events ^a (°C)	Total C ^b (%)	Thermal Events ^a (°C)	Total C ^b (%)
Mn	315.9	10.6	215.2	14.9
	541.0		450.1	
			603.2	
Fe	547.6	18.8	534.9	11.5
	205.1		216.3	
	384.5		384.7	
Ni	621.3	31.4	545.7	19.7
	635.2		630.2	
	567.0		570.1	
Cu	567.0	10.3	570.1	11.5
	577.7		414.9	
Zn	577.7	23.3	414.9	24.2
			557.6	

^a determined by the weight derivative curve (Fig. S4); ^b determined as the relation of total weight loss and the initial amount of M_{20} MMO weighted in the TGA crucible.

Table 2

Crystallite sizes for M_{20} MMO, before and after the reaction with IA and FO.

M_{20} MMO	Crystallite size, D (Å) ^a		
	Before Reaction	After Reaction	
		IA	FO
Mn	34.89	61.68	42.44
Fe	44.69	41.67	42.30
Co	41.13	43.84	39.00
Ni	43.77	39.25	42.84
Cu	41.07	85.85	90.88
Zn	40.52	48.46	34.07

^a calculated using the Scherrer equation.

conversion curve shapes for FO are different from the ones for IA, presenting an accentuated decrease in the first 120 min of reaction and then reaching a less drastic decrease until 360 min. The exception to the above behavior was Zn_{20} MMO, which presented a continuous decrease

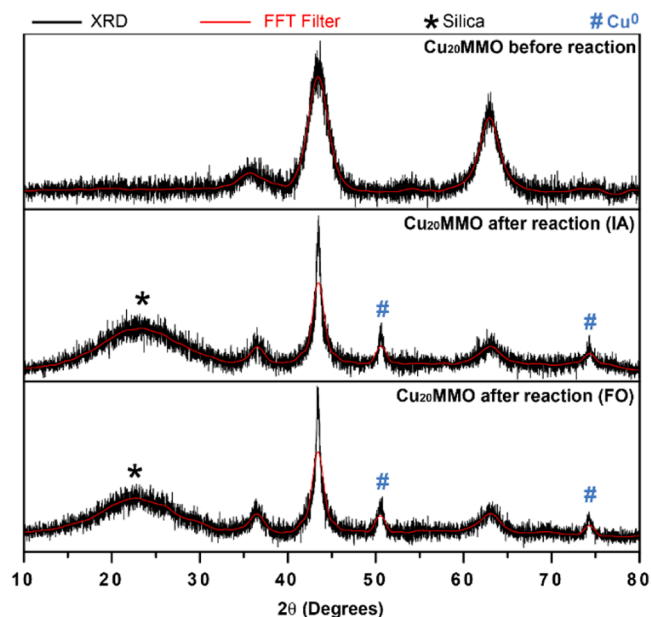


Fig. 5. XRD diffractograms for Cu_{20}MMO before and after reaction with IA and FO.

in FO conversion until 300 min.

The decrease in FO conversion to IA can be attributed to the matrix's complexity, as FO is a mixture of alcohols with different carbon chain lengths and reactivities. Thus, the decrease in the FO conversion may be related to carbon deposition over the catalyst surface during the reaction, by the CO and CH_4 reactions through the Boudouard mechanism [22,45,46], or by structural changes in the catalyst during the reactions, such as phase segregate on or changes in the oxidation state of the transition metals. To better understand the decrease in conversion value for the M_{20}MMO , *post-mortem* SEM, Raman, TGA, and XRD analyses were carried out to search for carbon deposits and structural changes.

3.3. Post-mortem M_{20}MMO analysis

Several analytical techniques, including SEM, Raman, TGA, and XRD, were used to better understand the deactivation mechanisms of M_{20}MMO catalysts after interactions with IA and FO. Notably, all catalyst specimens under the reaction with IA and FO changed color after the reactions, turning black, indicating the development of carbon deposits during the reactions. SEM examinations of Fe_{20}MMO and Zn_{20}MMO catalysts revealed different morphological changes caused by the IA and FO reactions (shown in Fig. 2). Among these observations is the formation of irregular agglomerates with flake-like features that diverge from the catalyst's initial structure.

EDS analysis of the samples revealed a small amount of carbon (approximately 3%) before the reactions that can be attributed to the samples' absorption of ambient CO_2 . However, carbon percentages increased significantly after the reactions, ranging from 16.0% to 31.7% depending on the sample (Table S2), implying that carbon deposits formed throughout the process. The SEM images were considerably different following the catalytic reactions of ethanol employing the same catalysts [25], where the formation of carbon nanotubes was observed during the reaction, which was not found for IA and FO.

Raman spectroscopy was utilized to examine the M_{20}MMO employed in the reactions. The catalysts were analyzed before the reactions and revealed minimal peaks, as expected for mixed metal oxides (Fig. S4). The Raman spectra of the M_{20}MMO after the reaction with IA and FO, on the other hand, were completely distinct as shown in Fig. 3.

The similarity of the spectra indicates that the same carbon deposition occurred in all samples after the reaction with IA and FO. The first-order Raman spectrum is in the range of $1000\text{--}1700\text{ cm}^{-1}$ (Fig. 3, A and B), and the second-order is in the range of $2300\text{--}3300\text{ cm}^{-1}$ [47–49]. The first-order Raman spectrum was adequately fitted to five bands, ascribed as D^* , D , D' , G , and D' [47,49]. An illustrative example is shown in Fig. 4 for the Zn_{20}MMO sample after reaction with FO. The shape of these bands and their relative positions and intensities provide significant information regarding the composition of the carbon material [47–49].

The superposition of the G and D' modes gives rise to an apparent G

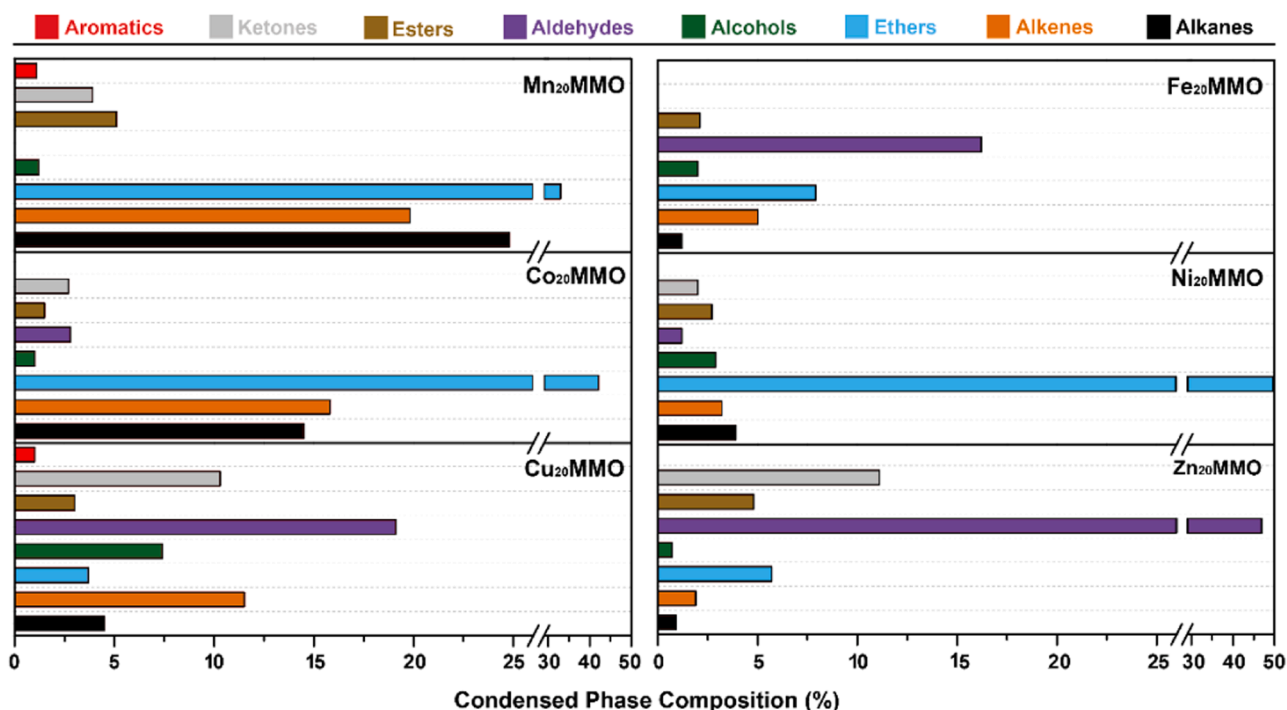


Fig. 6. Percentages for product class distribution for IA conversion for M_{20}MMO catalysts. The percentage values are the average for 6 h of reaction.

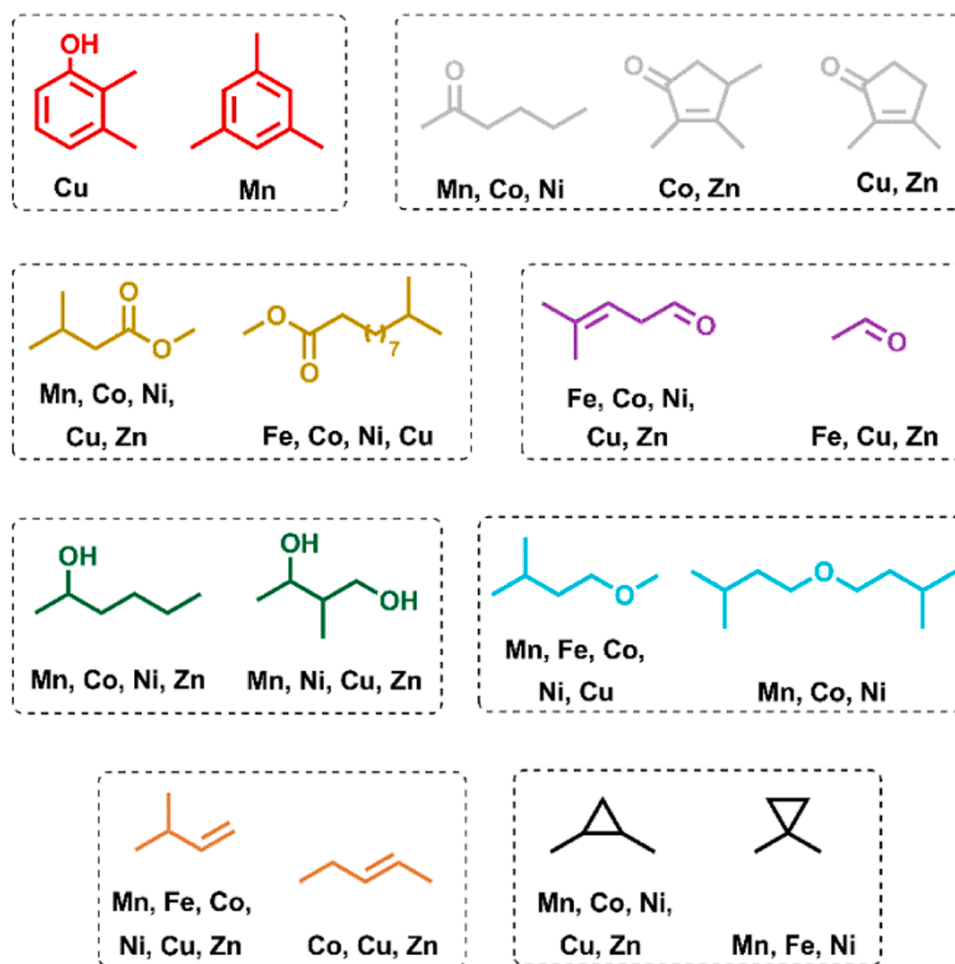


Fig. 7. Main products for each class obtained for the catalytic reaction of IA with $M_{20}MMO$. The element symbols below each structure represent the M^{2+} for $M_{20}MMO$.

peak, ascribed to G_{app} as shown in Fig. 4 [48]. The difference in the positions of the D' and G_{app} (i.e., $D' - G_{app}$) is associated with the graphene derivatives [48]. For $D' - G_{app} < 0$, the material is characterized as graphene oxide (GO), for $0 < D' - G_{app} < 25$, as reduced GO (rGO), and for $D' - G_{app} > 25$, as graphene [48]. The spectrum in Fig. 4 gives a value of $D' - G_{app} = 7$; therefore, this carbon deposition corresponds to rGO [48]. Similar results were obtained for the rest of the $M_{20}MMO$ after reactions with IA and FO, with $D' - G_{app}$ ranging from 5 to 9. Table S3 collects the band parameters obtained from the fits of all samples. Another feature that agrees with the previous analysis is the D^* band, Fig. 4, which has a significant increase in intensity in rGO samples [49] and that is seen as a shoulder at $\sim 1210\text{ cm}^{-1}$ in all the $M_{20}MMO$, Fig. 3, confirming the formation of rGO on the catalysts after the reaction with IA and FO. The Raman results are consistent with EDS analyses, which show carbon deposition on the catalyst's surface throughout the reaction course. Moreover, the Raman spectra of the $M_{20}MMO$ before the reaction with IA and FO (Fig.S4) do not have the characteristic bands observed after the reaction with IA and FO (Fig. 3), confirming that the carbon deposition occurs during the reaction course.

In addition to the SEM and Raman analyses, the $M_{20}MMO$ after the reaction was also subjected to TGA in order to identify the temperatures at which the rGO would oxidize and compare them with the literature, as well as the mass loss observed to quantify the carbon deposited on the surface of the catalyst. After the reactions with IA and FO, the catalysts were dried at $150\text{ }^{\circ}\text{C}$ for 12 h and kept in a desiccator. Any mass loss observed in the TGA is related to the oxidation of rGO to CO_x . It is important to recall that after TGA analysis, the black color observed for

all $M_{20}MMO$ disappeared, and the solids recovered their original colors, as shown in Fig.S5. The thermograms for $M_{20}MMO$ are shown in Fig.S6 and S7. The results for the reaction carried out with IA and FO are depicted in Table 1.

Comparing the IA and FO data in Table 1, the quantity of deposited rGO throughout the $M_{20}MMO$ varied widely. However, for some $M_{20}MMO$, the reaction with IA resulted in a more significant total rGO amount ($M^{2+} = \text{Co}$ and Ni). Furthermore, for $\text{Cu}_{20}MMO$ and $\text{Zn}_{20}MMO$, the percentage of total rGO quantity is nearly identical for both IA and FO, with a 1% difference. To determine if there was a relationship between the amount of rGO deposited and the amount of IA or FO converted, the percentages were plotted vs. conversion (average of 6 h of reaction), as shown in Fig.S8. There was no evident relationship between the two variables listed above for both IA and FO, indicating that the rGO deposited may not be the primary cause of the reduced conversion found for FO compared to IA.

The $M_{20}MMO$ were also submitted to XRD analysis after the reactions. Using the diffractograms depicted in Figs. S9 and S10, the crystallite sizes (D) were calculated for the $M_{20}MMO$ before and after the reaction. Table 2 resumes the values.

Considering the values resumed in Table 2, there was no clear relationship regarding the IA or FO for D values before and after the reaction. However, the $\text{Mn}_{20}MMO$ and $\text{Cu}_{20}MMO$ presented a substantial increase in D values, mainly for the Cu catalyst. The increase in the D value may be associated with particle aggregation during the reaction that generates clusters [25]. The same behavior was observed before for the MMO catalytic transformation of ethanol into 1-butyl alcohol [25].

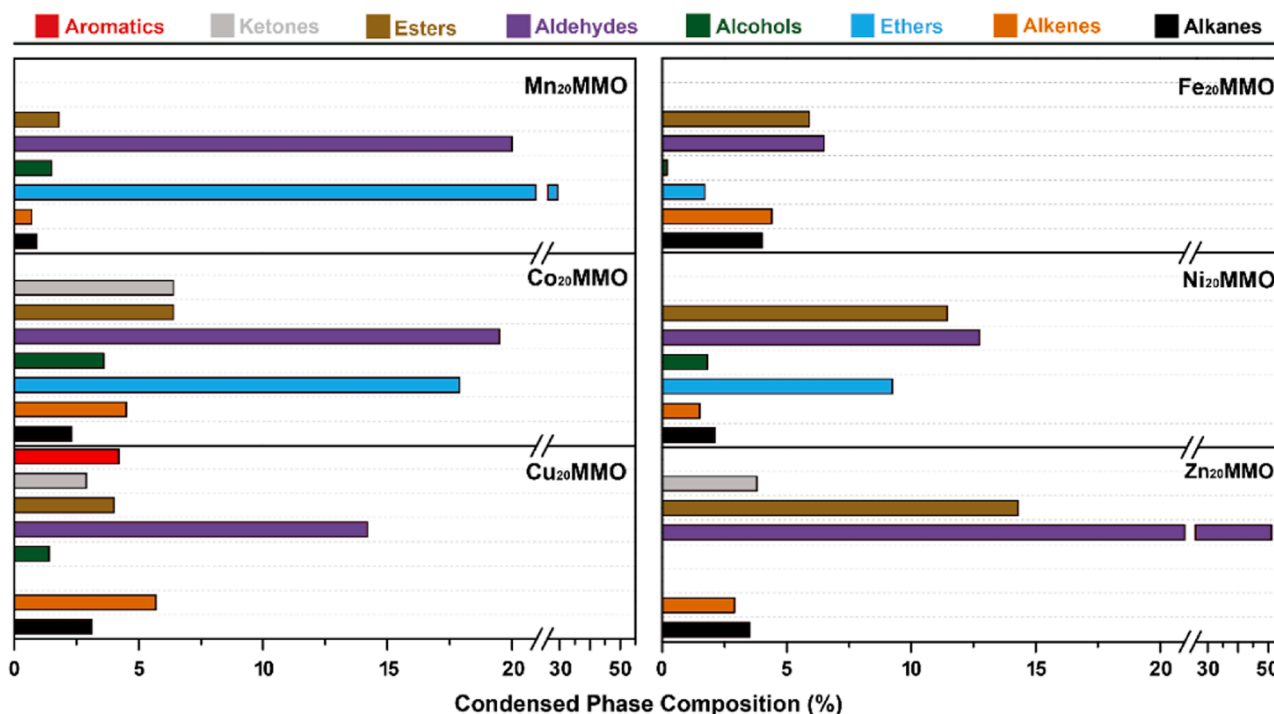


Fig. 8. Percentages for product class distribution for FO conversion for M_{20} MMO catalysts. The percentage values are the average for 6 h of reaction.

Regarding the XRD fingerprint for MMO, only the catalyst Cu_{20} MMO showed structural changes, with two new diffraction peaks at 50.4 and 74.4° for both IA and FO reactions. When these peaks are compared to the ICDD diffractogram database, they are consistent with the formation of Cu^0 species (JCPDS 003–1018), as seen in Fig. 5.

The reduction of $Cu(II)$ to $Cu(0)$ present in the Cu_{20} MMO structure can be attributed to the presence of H_2 inside the reactor due to the reforming and dehydrogenation reactions of the alcohols [31]. The change in the Cu redox state may be the driving force for the modification in the catalyst structure. It may be tentatively attributed to the higher values of D observed for the Cu catalyst in Table 2. However, the other M_{20} MMO did not present extra diffraction peaks, indicating that the redox process did not occur or that the amount of reduced metal species was insufficient to be detected by XRD.

3.4. Isoamyl alcohol (IA): distribution by class and main products

The reaction IA over M_{20} MMO produced *c.a.* 30 different products, distributed in 8 classes: aromatics, ketones, esters, aldehydes, alcohols, ethers, alkanes, and alkenes. The percentage distribution of each class was directly influenced by the transition metal ion that partially substituted the Mg^{2+} in the structure. Fig. 6 shows the distribution by class for each M_{20} MMO.

Ethers were the main products for $M^{2+} = Mn, Co,$ and Ni , while aldehydes were the main products for $M^{2+} = Fe, Cu,$ and Zn . The formation of ethers is related to the dehydration reaction involving two molecules of alcohol and the obtention of aldehydes is due to dehydrogenation of one molecule of alcohol. The presence of unsaturated aldehydes, mostly 2,4-dienals, is related to forming aromatic compounds in small quantities for $M^{2+} = Fe$ and Cu .

Esters were also found, in a small percentage, for all M_{20} MMO. The formation of esters may be attributed to the oxidative esterification of one aldehyde and one alcohol molecule. The esters were found in higher percentages for $M^{2+} = Ni, Cu,$ and Zn .

Alkanes and alkenes are two further types of chemicals produced by all M_{20} MMO but in different quantities. Alkenes are formed by dehydrating a single alcohol molecule, whereas alkanes are produced via

hydrodeoxygenation (HDO). Alkanes and alkenes were found as products for all M_{20} MMO but in more significant percentages for $M^{2+} = Mn, Co,$ and Cu .

The ketones are also present as products in all catalysts, except for Fe_{20} MMO, and in high percentages for $M^{2+} = Cu,$ and Zn . The possible mechanism for its formation was proposed as a decarboxylation and dehydrogenation reaction after the condensation of one molecule of alcohol and one of aldehyde [50]. Furthermore, cyclic ketones may be due to the cyclization of unsaturated ketones or di-ketones. Finally, alcohol was also found among the identified products. The alcohols were found in small percentages in all M_{20} MMO. The formation of alcohols can be attributed to the condensation of two aldehyde molecules and subsequent hydrogenation.

The main products for each class are depicted in Fig. 7. The percentages for each and all the minor products are depicted in Tables S4 to S15.

Considering the product structures depicted in Fig. 7, in some cases, the number of carbon atoms is higher than the five expected for the reaction of IA or methanol, the two initial reactants. Also, the number of carbon atoms did not match the combination of the reactants (for example, the self-condensation of IA would give a chain of 10 carbon atoms). For aromatics, ketones, esters, aldehydes, and alcohols, the number of carbon atoms varies from C_6 to C_{12} . Also, a considerable amount of acetaldehyde was found in the aldehyde class of compounds, which has a lower number of carbons in the structure than five. Thus, the number of carbon atoms found in some of the products may suggest radical reactions on the catalyst surface.

The temporal behavior for each class of products for all M_{20} MMO is shown in Fig. S11. For all catalysts, the first 30 min of reaction corresponded to the maximum production of a distinct class of compounds. After 30 min, the production usually diminished to low percentage values and was kept almost constant until 360 min. The exceptions were Co_{20} MMO, which increased ether production after 120 min, and Ni_{20} MMO, which kept the production of ether *c.a.* 50% until 360 min. Also, for Cu_{20} MMO, the aldehydes decreased after 240 min, and the alkenes increased after 180 min. The decrease in the percentage of condensed products, except for Co_{20} MMO, may indicate that in the first

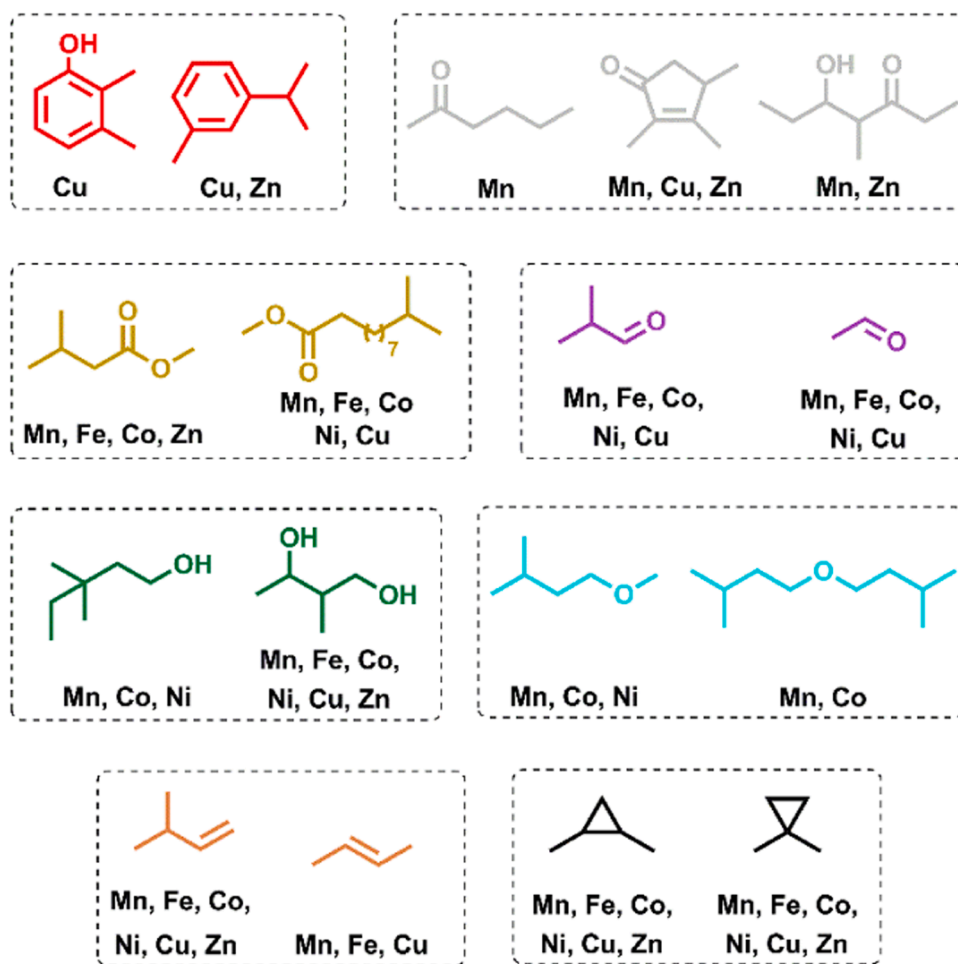


Fig. 9. Main products for each class obtained for the catalytic reaction of FO with $M_{20}MMO$. The element symbols below each structure represent the M^{2+} for $M_{20}MMO$.

initial three min of the reaction, the catalyst surface and the favored reaction pathway over it are changing. Thus, the initial 30 min of reaction stabilize the catalyst surface for further reactions. However, as shown in Fig. 1, the IA conversion diminishes for all catalysts during the 360 min of reaction. Thus, it may not be excluded that the catalyst's deactivation process also contributes to the change in the temporal behavior of the products.

3.5. Fusel Oil (FO): distribution by class and main products

The change of IA for FO for the reaction over the $M_{20}MMO$ showed a distinct behavior over the products class distribution, as shown in Fig. 8. The number of products and the class of products found for FO were lower than for IA. As already depicted in Fig. 1, the conversion of FO into condensed products was also lower than the ones found for IA.

Using FO instead of IA increased the production of aldehydes for all $M_{20}MMO$, mostly for $M^{2+} = Mn$ and Ni , and the high production of ethers observed for IA was supplanted by aldehydes. Also, the percentages of ketones, alcohols, alkenes, and alkanes for FO were lower than the ones found for IA for all $M_{20}MMO$. However, in the opposite direction of the above trend, the percentage of esters increased for all catalysts, being the second most abundant product class for $M^{2+} = Fe, Ni$, and Zn . Also, the percentage of aromatics increased considerably for $Cu_{20}MMO$ and decreased for the $Mn_{20}MMO$. Fig. 9 summarizes the main products identified for each class, and all the minor products are depicted in Tables S4 to S15.

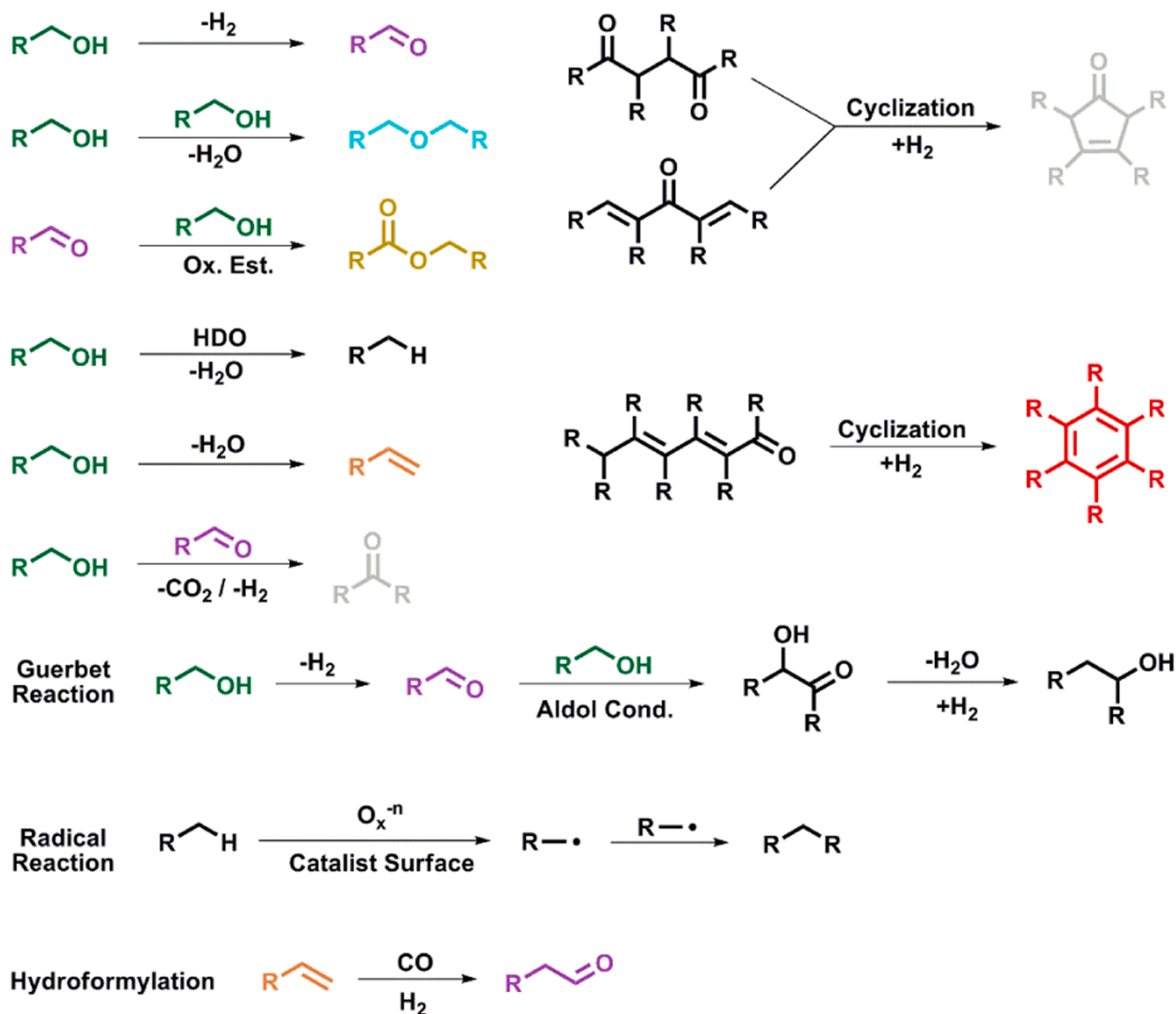
The increase in the production of aldehydes and ester may be related

to the complexity of the FO since it is a mixture of four alcohols (ethyl, 1-butyl, isobutyl, and isoamyl) and also 30% (v/v) of methanol. Thus, five distinct substrates compete for the same number of active sites of the $M_{20}MMO$, diminishing the probability of further reactions to produce more complex products such as ketones and aromatics. The high percentage of aldehydes produced, which are obtained from the dehydrogenation reaction, contributes to the hypothesis above.

Comparing the temporal behavior of each product class using the same catalyst, FO instead of IA (Fig. S12) kept the exact pattern of high production of a selected compound class in the first 30 min of the reaction. However, due to the lower FO conversion, the percentage of each class until 360 min was lower than that obtained for IA. Considering each catalyst, the $Mn_{20}MMO$ presented an exponential growth for the aldehydes and esters and a bell shape for ketones that were not observed for the IA. The same bell shape was observed for the aldehydes using $Co_{20}MMO$ as a catalyst. For $Zn_{20}MMO$, it was observed that a bell-shaped curve for the ketones, exponential growth for esters, and exponential decay for the aldehydes reached a plateau at 300 min. For the other catalysts, the temporal behavior for the product classes identified was almost the same as that observed for IA but with lower relative percentages.

4. Discussion

Observing exponential growth and decline of the product classes during the reaction time frame (Fig. S11 and S12) can suggest a relationship between the formation and consumption. In contrast, the bell-



Scheme 1. Proposed reactions and pathways to reach the identified products.

shaped curve can indicate the formation and consumption of reaction intermediates. However, the kinetic treatment of the data is not feasible due to the number of products found and the difficulty in attributing the specific reaction mechanism to the reactions occurring on the catalyst surface. However, it is possible to create a hypothesis for the reactions that may occur as a function of the products. Scheme 1 resumes the proposed reactions to reach the products depicted in Figs. 7 and 9.

The formation of aldehydes, ethers, esters, alkenes, and aliphatic ketones can be explained by dehydrogenation, dehydration, oxidation, and decarboxylation reactions, as shown in Scheme 1. Cyclization and hydrogenation reactions may explain the formation of cyclic ketones and aromatics through the previous formation of diketone, 2,5-dien-4-one, and 2,4-dienal intermediates. None of these intermediates could be identified by GC-MS, suggesting that the amount formed of these intermediates is low and the cyclization and hydrogenation occur quickly. Another product that deserves attention is acetaldehyde. In the $M_{20}MMO$, which presented aldehyde production, it was the second most abundant one. However, it is a C_2 aldehyde, and even for FO, the relative percentage of ethanol in the mixture is 1.5%, which is incompatible with the relative percentage of acetaldehyde found in the condensed

products. The presence of methanol in the reactor could be responsible for forming formaldehyde, which could be a reactive intermediate for the Guerbet reaction. However, there is no aldol condensation reaction between methanol and formaldehyde. Thus, one possibility would be methanol hydroformylation since, due to the alcohol reforming reaction, carbon monoxide is available to react.

The carbon chain growing through carbon-carbon bond formation may be related to Aldol condensation in a Guerbet-type reaction or through a radical reaction pathway. For example, it was identified among the products with carbon chains ranging from C_6 to C_{12} . These carbon chains may combine IA and methanol (C_5 and C_1 through Aldol condensation to produce C_6) and a combination of the products with the starting alcohols. As already reported for mixed metal oxides, the carbon-carbon may also be formed by radical reactions on the catalyst surface [51–53]. One possible pathway may be alcohol hydrodeoxygenation (HDO) [54], resulting in the correspondent alkane, which may undergo hydrogen abstraction by oxygen species over the catalyst, giving rise to the respective carbon-centered radical. Although less probable, the radical formation hypothesis may be important to explain the production of some products that the Aldol condensation

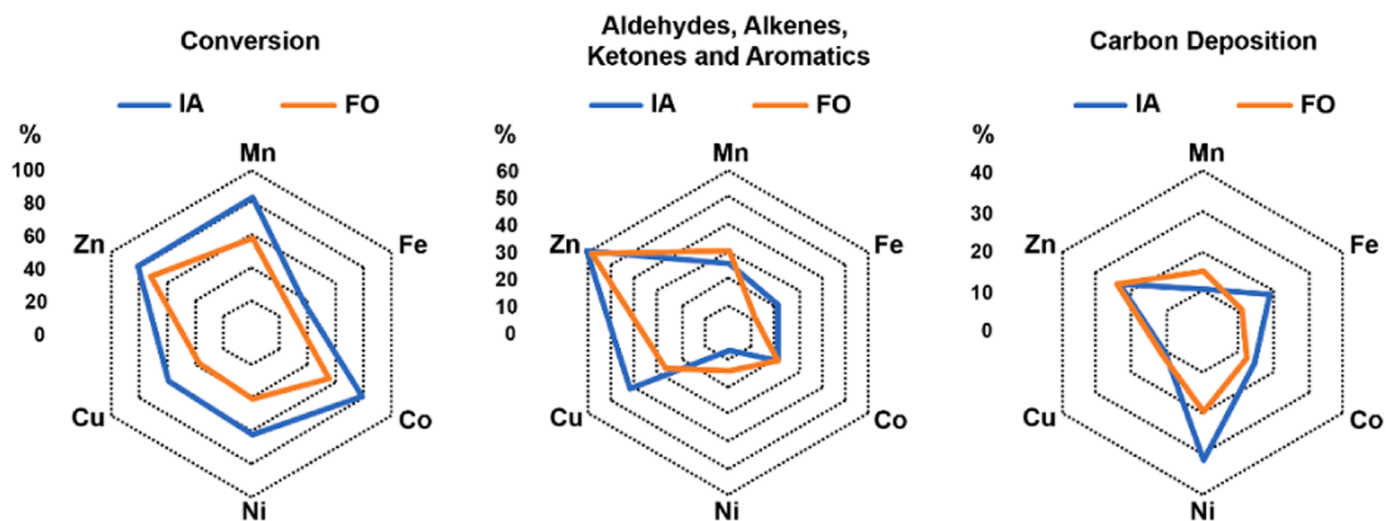


Fig. 10. Comparison of substrate conversion, selected products on the condensed phase and carbon deposition for $M_{20}MMO$.

cannot achieve. It was reported that the condensation of two molecules of 1-butyl alcohol to give the respective C_8 alcohols did not occur over $Cu_{20}MMO$ [26]. Instead of the long-chain alcohol, aromatics, ketones, and carbonyl compounds were observed. The non-condensation was attributed to steric hindrance in forming the Aldolic intermediate.

The above discussion about the mechanisms and pathways to reach the identified products indicates the complexity of the reaction framework to convert IA or FO into high-added value products. The catalyst must perform multiple reactions such as hydro- and dehydrogenation, HDO, dehydration, and decarboxylation to generate the products and the reactive intermediate for the more complex molecules. Thus, the $M_{20}MMO$ is the right platform to develop IA and FO transformations due to its proven versatility. However, due to the need for multiple-type reactions, the selectivity for a lower number of products is sacrificed in favor of reactivity, which mainly for FO transformation proved to be an issue due to decreased conversion over time. Thus, optimizing the catalyst and the process will continuously improve the following studies on IA and FO. To circumvent the selectivity issue, the products identified could be separated by distillation, but further studies and simulations must be carried out to validate the energetic and economic viability of the process. Also, further studies must be conducted to determine the viability of separating IA from FO and its further utilization in the catalytic process instead of the more complex initial matrix.

Taking into account the data of the catalytic transformation of IA and FO over the $M_{20}MMO$, it is important to analyze the role of the M^{2+} in at least three parameters: substrate conversion, production of unsaturated and carbonyl compounds as products (aldehydes, alkenes, ketones, and aromatics), which are highly desirable for other reactions as organic building blocks, and carbon deposition over the catalyst surface during the reactor operation. Fig. 10 resumes this information.

Analyzing the conversion of IA and FO, the catalysts where $M^{2+} = Mn, Co$, and Zn can be highlighted as the ones with higher percentages. Also, considering the shape of the curves, it is possible to observe that $M^{2+} = Cu$ and Mn had a higher proportional decrease in the conversion percentage in the change of IA for FO, indicating that both metals were more sensitive to the substrate change. Considering the unsaturated and carbonyl production, $M^{2+} = Cu$ and Zn deserve attention, with c.a. 40 and 60% of aldehydes, alkenes, ketones, and aromatics in the condensed phase composition. Also, for $M^{2+} = Zn$, there was no significant change in the percentage changing IA by FO, which was not observed for the Cu -containing catalyst. For the last parameter, the carbon deposition, the catalysts containing $M^{2+} = Fe, Ni$, and Zn presented higher percentages. It is important to recall that $M^{2+} = Fe$ combined a low substrate conversion with a high carbon deposition, indicating that the reaction

pathways for carbon formation are highly active for this metal. Considering the conversion and carbon deposition ratio, $M^{2+} = Fe$ and Ni and $M^{2+} = Mn$ and Co had the worst and best behavior, respectively. Thus, combining the three parameters, the $Zn_{20}MMO$ presented the best performance, although the carbon deposition over the catalyst can become an issue in long-term reactor operation.

The obtention of aldehydes, ketones, alkenes, and aromatic compounds from a renewable and underutilized carbon source is crucial in considering greener reaction routes for raw chemicals. The initial aim of the catalytic transformation of IA and FO into organic building blocks was achieved using $M_{20}MMO$ as a catalyst. The classes of compounds mentioned above are crucial intermediates for many organic synthetic industrial processes due to the presence of carbonyl and olefinic bonds. Also, the ethers and polyols can be used as solvents or polymer precursors, and the esters can be applied as flavoring agents.

5. Conclusions

In conclusion, our work successfully proved the catalytic conversion of isoamyl alcohol (IA) and fusel oil (FO) into valuable organic compounds with carbon chains ranging from C_6 to C_{12} . This transformation, performed at $550^\circ C$ in an atmospheric pressure fixed bed flow reactor, relied on mixed metal oxides ($M_{20}MMO$) as catalysts. The individual M^{2+} ions ($M^{2+} = Mn, Fe, Co, Ni, Cu$, and Zn) that partially replaced Mg^{2+} (20 mol%) were critical in determining IA and FO conversions and product distribution. This selective substitution of M^{2+} ions controlled the desired product class or type. Among the various catalysts investigated, $Zn_{20}MMO$ emerged as the most promising performer, exhibiting superior results in substrate conversion, unsaturated and carbonyl compound production, and mitigation of carbon deposition on the catalyst surface throughout the reaction. Although there was some indication of reduced graphene oxide generation on the catalyst surface after 6 h of reaction due to partial reforming reactions of the substrates into gaseous compounds, these phenomena lacked a strong association with declining substrate consumption with time. Regarding catalyst structural stability, the XRD patterns of the $M_{20}MMO$ catalysts remained substantially unchanged after 6 h of reaction, except for $M^{2+} = Cu$, which formed a unique Cu^0 phase demonstrating the $M_{20}MMO$ catalysts' durability for sustained IA and FO catalytic conversions, as structural modifications were minor. Notably, the study found a difference in conversion behavior between IA and FO, with FO observing a faster drop-in conversion rate. This disparity highlights the impact of FO's complex matrix on catalytic activity. The findings of this study provide effective evidence of fusel oil's potential as a renewable carbon source

capable of producing important organic building blocks with a wide range of applications.

CRedit authorship contribution statement

Jorge Andrés Mora Vargas: Data curation, Investigation, Methodology. **Livia Padilha de Lima:** Data curation, Investigation, Methodology. **Rafael Francisco Cassaro:** Data curation, Investigation, Methodology. **Felipe Garcia da Silva:** Data curation, Investigation, Methodology. **Julieth Orduna Ortega:** Data curation, Investigation, Methodology. **Antonio Carlos Roveda Jr:** Data curation, Investigation, Methodology. **Gustavo Metzker:** Conceptualization, Supervision, Writing – original draft, Writing – review & editing. **Mauricio Boscolo:** Conceptualization, Funding acquisition, Project administration, Writing – original draft. **Daniel Rodrigues Cardoso:** Data curation, Writing – review & editing.

Declaration of Competing Interest

The authors declare that they have no known competing financial interests or personal relationships that could have appeared to influence the work reported in this paper.

Data availability

Data will be made available on request.

Acknowledgments

The authors, especially MB, acknowledge the Sao Paulo State Research Foundation – FAPESP (grant number 2020/02471-4) for the financial support. JAMV also acknowledge Universidad Santiago de Cali for Joven Investigador Santiaguino fellowship (convocatoria interna DGI No. 06-2023) and for the financial support (Proyecto No. 939-621121-2827). JOO acknowledge Universidad Santiago de Cali for the doctoral fellowship. ACRJ acknowledge FAPESP for post-doc fellowship (grant number 2021/13985-1). DRC is thankful to CNPq for the research productivity fellowship. G.M acknowledge Coordination for the Improvement of Higher Education Personnel – CAPES for the post-doc fellowship (grant number 1760327). We also acknowledge Professor Peter C. Ford (University of California, Santa Barbara) for carefully reading and suggestions on the manuscript.

Appendix A. Supporting information

Supplementary data associated with this article can be found in the online version at [doi:10.1016/j.apcatb.2024.123985](https://doi.org/10.1016/j.apcatb.2024.123985).

References

- [1] UNICA - Brazilian Sugarcane Industry and Bioenergy Association, (2023). (<https://unica.com.br/en/>).
- [2] G. Metzker, J.A.M. Vargas, M. Boscolo, Heterogeneous catalytic ethanol transformation into chemicals: some Brazilian contributions, in: P.C. Ford, R. van Eldik (Eds.), *Adv. Inorg. Chem.*, Academic Press in a imprint of Elsevier, 2021, pp. 343–375.
- [3] P.E. Fernando Santos, Sarita Candida Rabelo, Mario de Matos, ed., *Sugarcane Biorefinery, Technology and Perspectives*, Academic Press in a imprint of Elsevier, 2020.
- [4] Q.U.A. Raza, M.A. Bashir, A. Rehim, M.U. Sial, H.M.A. Raza, H.M. Atif, A.F. Brito, Y. Geng, Sugarcane industrial byproducts as challenges to environmental safety and their remedies: a review, *Water (Switzerland)* 13 (2021) 1–19, <https://doi.org/10.3390/w13243495>.
- [5] J. Orduña Ortega, J.A. Mora Vargas, O.M. Perrone, G. Metzker, E. Gomes, R. da Silva, M. Boscolo, Soaking and ozonolysis pretreatment of sugarcane straw for the production of fermentable sugars, *Ind. Crops Prod.* 145 (2020) 111959, <https://doi.org/10.1016/j.indcrop.2019.111959>.
- [6] J.O. Ortega, J.A. Mora Vargas, G. Metzker, E. Gomes, R. da Silva, M. Boscolo, Enhancing the production of the fermentable sugars from sugarcane straw: a new approach to applying alkaline and ozonolysis pretreatments, *Renew. Energy* 164 (2021) 502–508, <https://doi.org/10.1016/j.renene.2020.09.070>.
- [7] C.A. Christoforetti, J.P. Escher, J.E. Correia, J.F.U. Marinho, C.S. Fontanetti, Sugarcane vinasse: environmental implications of its use, *Waste Manag* 33 (2013) 2752–2761, <https://doi.org/10.1016/j.wasman.2013.09.005>.
- [8] J. de J. Mendoza-Pedroza, E. Sánchez-Ramírez, J.G. Segovia-Hernández, S. Hernández, A. Orjuela, Recovery of alcohol industry wastes: revaluation of fusel oil through intensified processes, *Chem. Eng. Process. - Process. Intensif.* 163 (2021) 0–6, <https://doi.org/10.1016/j.cep.2021.108329>.
- [9] A.V. Chistyakov, M.V. Tsodikov, M.V. Chudakova, M.A. Gubanov, P.A. Zharova, Z. M. Bukina, N.V. Kolesnichenko, A.E. Gekhman, S.N. Khadzhev, Direct conversion of ethanol and fusel oils to alkane-aromatic hydrocarbons in the presence of a pilot Pd–Zn/TsVM catalyst, *Pet. Chem.* 58 (2018) 32–42, <https://doi.org/10.1134/S096554411801005X>.
- [10] S.M. Safieddin Ardebili, H. Solmaz, D. İpci, A. Calam, M. Mostafaei, A review on higher alcohol of fusel oil as a renewable fuel for internal combustion engines: applications, challenges, and global potential, *Fuel* 279 (2020), <https://doi.org/10.1016/j.fuel.2020.118516>.
- [11] M.E. Dias De Oliveira, B.E. Vaughan, E.J. Rykiel, Ethanol as fuel: energy, carbon dioxide balances, and ecological footprint, *Bioscience* 55 (2005) 593–602, [https://doi.org/10.1641/0006-3568\(2005\)055\[0593:EAFEDC\]2.0.CO;2](https://doi.org/10.1641/0006-3568(2005)055[0593:EAFEDC]2.0.CO;2).
- [12] T. Massa, D. Raspe, M. Feiten, L. Cardozo-Filho, C. da Silva, Fusel oil: chemical composition and an overview of its potential application, *J. Braz. Chem. Soc.* 34 (2023) 153–166, <https://doi.org/10.21577/0103-5053.20220145>.
- [13] M.C. Ferreira, A.J.A. Meirelles, E.A.C. Batista, Study of the fusel oil distillation process, *Ind. Eng. Chem. Res.* 52 (2013) 2336–2351, <https://doi.org/10.1021/ie300665z>.
- [14] O.I. Awad, O.M. Ali, A.T. Hammid, R. Mamat, Impact of fusel oil moisture reduction on the fuel properties and combustion characteristics of SI engine fueled with gasoline-fusel oil blends, *Renew. Energy* 123 (2018) 79–91, <https://doi.org/10.1016/j.renene.2018.02.019>.
- [15] S. Özer, The effect of diesel fuel-tall oil/ethanol/methanol/isopropyl/n-butanol/fusel oil mixtures on engine performance and exhaust emissions, *Fuel* 281 (2020) 118671, <https://doi.org/10.1016/j.fuel.2020.118671>.
- [16] A.L.B. Dias, T. Hatami, J. Martínez, O.N. Ciftci, Biocatalytic production of isoamyl acetate from fusel oil in supercritical CO₂, *J. Supercrit. Fluids* 164 (2020), <https://doi.org/10.1016/j.supflu.2020.104917>.
- [17] A.L.B. Dias, A. Ubeyitogullari, T. Hatami, J. Martínez, O.N. Ciftci, Continuous production of isoamyl acetate from fusel oil under supercritical CO₂: a mass transfer approach, *Chem. Eng. Res. Des.* 176 (2021) 23–33, <https://doi.org/10.1016/j.cherd.2021.09.026>.
- [18] P. Patidar, S.M. Mahajani, Esterification of fusel oil using reactive distillation - Part I: Reaction kinetics, *Chem. Eng. J.* 207–208 (2012) 377–387, <https://doi.org/10.1016/j.cej.2012.06.139>.
- [19] T.T.V. Tran, S. Kongparakul, S. Karnjanakom, P. Reubroycharoen, G. Guan, N. Chanlek, C. Samart, Selective production of green solvent (isoamyl acetate) from fusel oil using a sulfonic acid-functionalized KIT-6 catalyst, *Mol. Catal.* 484 (2020) 110724, <https://doi.org/10.1016/j.mcat.2019.110724>.
- [20] E.R. Pérez, N.C. Carnevalli, P.J. Cordeiro, U.P. Rodrigues-Filho, D.W. Franco, Efficient solvent-free microwave-assisted esterification of fusel oil using p-tsoh and h₃pw12o₄₀ as catalysts, *Org. Prep. Proced. Int.* 33 (2021) 395–400, <https://doi.org/10.1080/00304940109356609>.
- [21] S. Sumrunnonnasak, P. Reubroycharoen, N. Pimpha, N. Chanlek, S. Tantayanon, Hydrogen production by steam reforming of fusel oil using a CeCoO_x mixed-oxide catalyst, *Chem. Eng. Technol.* 43 (2020) 689–697, <https://doi.org/10.1002/ceat.201900423>.
- [22] T.H. Le-Mai, S. Mhadmhan, T.Q. Trieu, N. Prasongthum, P. Suriya, P. Reubroycharoen, Hydrogen production by steam reforming of fusel oil over Ni-based fiber catalyst, *Mater. Today Proc.* 57 (2022) 1147–1153, <https://doi.org/10.1016/j.matpr.2021.10.012>.
- [23] R. Yaisamlee, P. Reubroycharoen, Light olefin production from the catalytic cracking of fusel oil in a fixed bed reactor, *Biomass Bioenergy* 153 (2021) 106217, <https://doi.org/10.1016/j.biombioe.2021.106217>.
- [24] P.A. Chistyakova, A.V. Chistyakov, S.A. Nikolaev, R.A. Bagdatov, M.V. Tsodikov, J. Heider, A.I. Netrusov, Conversion of ethanol and fusel oils over Au–M/MFI/Al₂O₃ catalysts, *Pet. Chem.* 62 (2022) 1107–1125, <https://doi.org/10.1134/S0965544122090018>.
- [25] G. Metzker, J.A. Mora Vargas, L.P. de Lima, O.M. Perrone, M.R. Siqueira, L. C. Varanda, M. Boscolo, First row transition metals on the ethanol Guerbet reaction: products distribution and structural behavior of mixed metal oxides as catalysts, *Appl. Catal. A Gen.* 623 (2021) 118272, <https://doi.org/10.1016/j.apcata.2021.118272>.
- [26] J. Mora Vargas, L.H. Tofaneli Morelato, J. Orduña Ortega, M. Boscolo, G. Metzker, Upgrading 1-butanol to unsaturated, carbonyl and aromatic compounds: a new synthesis approach to produce important organic building blocks, *Green. Chem.* 22 (2020) 2365–2369, <https://doi.org/10.1039/d0gc00254b>.
- [27] T. Kella, A.A. Vennathan, S. Dutta, S.S. Mal, D. Shee, Selective dehydration of 1-butanol to butenes over silica supported heteropolyacid catalysts: mechanistic aspect, *Mol. Catal.* 516 (2021) 111975, <https://doi.org/10.1016/j.mcat.2021.111975>.
- [28] J.A. Barrett, Z.R. Jones, C. Stickelmaier, N. Schopp, P.C. Ford, A pinch of salt improves n-butanol selectivity in the guerbet condensation of ethanol over Cu-doped Mg/Al oxides, *ACS Sustain. Chem. Eng.* 6 (2018) 15119–15126, <https://doi.org/10.1021/acssuschemeng.8b03589>.
- [29] D. Gabriëls, W.Y. Hernández, B.F. Sels, P. Van Der Voort, A. Verberckmoes, Review of catalytic systems and thermodynamics for the Guerbet condensation reaction and challenges for biomass valorization, *Catal. Sci. Technol.* 5 (2015) 3876–3902, <https://doi.org/10.1039/c5cy00359h>.

- [30] Z. Sun, A.C. Vasconcelos, G. Bottari, M.C.A. Stuart, G. Bonura, C. Cannilla, F. Frusteri, K. Barta, Efficient catalytic conversion of ethanol to 1-butanol via the guerbet reaction over copper- and nickel-doped porous, *ACS Sustain. Chem. Eng.* 5 (2017) 1738–1746, <https://doi.org/10.1021/acsschemeng.6b02494>.
- [31] M. Rechi Siqueira, O. Micali Perrone, G. Metzker, D.C. de Oliveira Lisboa, J. C. Thoméo, M. Boscolo, Highly selective 1-butanol obtained from ethanol catalyzed by mixed metal oxides: reaction optimization and catalyst structure behavior, *Mol. Catal.* 476 (2019) 110516, <https://doi.org/10.1016/j.mcat.2019.110516>.
- [32] J. de Souza Rossi, O.M. Perrone, M.R. Siqueira, D.P. Volanti, E. Gomes, R. Da-Silva, M. Boscolo, Effect of lanthanide ion doping on Mg–Al mixed oxides as active acid–base catalysts for fatty acid ethyl ester synthesis, *Renew. Energy* 133 (2019) 367–372, <https://doi.org/10.1016/j.renene.2018.10.038>.
- [33] O.M. Perrone, F. Lobefaro, M. Aresta, F. Nocito, M. Boscolo, A. Dibenedetto, Butanol synthesis from ethanol over CuMgAl mixed oxides modified with palladium (II) and indium (III), *Fuel Process. Technol.* 177 (2018) 353–357, <https://doi.org/10.1016/j.fuproc.2018.05.006>.
- [34] O.M. Perrone, M.R. Siqueira, G. Metzker, D.C. de Oliveira Lisboa, M. Boscolo, Copper and lanthanum mixed oxides as catalysts for ethanol Guerbet coupling: the role of La³⁺ on the production of long-chain alcohols, *Environ. Prog. Sustain. Energy* 40 (2021), <https://doi.org/10.1002/ep.13541>.
- [35] M.B. Gawande, R.K. Pandey, R.V. Jayaram, Role of mixed metal oxides in catalysis science - Versatile applications in organic synthesis, *Catal. Sci. Technol.* 2 (2012) 1113–1125, <https://doi.org/10.1039/c2cy00490a>.
- [36] G.S. MacAla, A.W. Robertson, C.L. Johnson, Z.B. Day, R.S. Lewis, M.G. White, A. V. Iretskii, P.C. Ford, Transesterification catalysts from iron doped hydrotalcite-like precursors: solid bases for biodiesel production, *Catal. Lett.* 122 (2008) 205–209, <https://doi.org/10.1007/s10562-008-9480-y>.
- [37] J.T. Kozlowski, R.J. Davis, Heterogeneous catalysts for the guerbet coupling of alcohols, *ACS Catal.* 3 (2013) 1588–1600, <https://doi.org/10.1021/cs400292f>.
- [38] A. Chierigato, J.V. Ochoa, C. Bandinelli, G. Fornasari, F. Cavani, M. Mella, On the chemistry of ethanol on basic oxides: revising mechanisms and intermediates in the lebedev and guerbet reactions, *ChemSusChem* 8 (2015) 377–388, <https://doi.org/10.1002/cssc.201402632>.
- [39] F. Cavani, F. Trifirò, A. Vaccari, Hydrotalcite-type anionic clays: preparation, properties and applications, *Catal. Today* 11 (1991) 173–301, [https://doi.org/10.1016/0920-5861\(91\)80068-K](https://doi.org/10.1016/0920-5861(91)80068-K).
- [40] M. Chui, G. Metzker, C.M. Bernt, A.T. Tran, A.C.B. Burtoloso, P.C. Ford, Probing the lignin disassembly pathways with modified catalysts based on Cu-doped porous metal oxides, *ACS Sustain. Chem. Eng.* (2017), <https://doi.org/10.1021/acsschemeng.6b02954>.
- [41] B.F. Sels, D.E. De Vos, P.A. Jacobs, Hydrotalcite-like anionic clays in catalytic organic reactions, *Catal. Rev. - Sci. Eng.* 43 (2001) 443–488, <https://doi.org/10.1081/CR-120001809>.
- [42] E. Conteroso, V. Gianotti, L. Palin, E. Boccaleri, D. Viterbo, M. Milanese, Facile preparation methods of hydrotalcite layered materials and their structural characterization by combined techniques, *Inorg. Chim. Acta* 470 (2018) 36–50, <https://doi.org/10.1016/j.ica.2017.08.007>.
- [43] J.M. Fernandez, C. Barriga, M. Ulibarri, F.M. Labajos, Preparation and thermal stability of manganese-containing, *J. Mater. Chem.* 4 (1994) 1117–1121.
- [44] J.C. Villegas, O.H. Giraldo, K. Laubernds, S.L. Suib, New layered double hydroxides containing intercalated manganese oxide species: Synthesis and characterization, *Inorg. Chem.* 42 (2003) 5621–5631, <https://doi.org/10.1021/ic030054k>.
- [45] D. Ayillath Kutteri, I.W. Wang, A. Samanta, L. Li, J. Hu, Methane decomposition to tip and base grown carbon nanotubes and CO_x-free H₂ over mono- and bimetallic 3d transition metal catalysts, *Catal. Sci. Technol.* 8 (2018) 858–869, <https://doi.org/10.1039/c7cy01927k>.
- [46] A. Ochoa, J. Bilbao, A.G. Gayubo, P. Castaño, Coke formation and deactivation during catalytic reforming of biomass and waste pyrolysis products: a review, *Renew. Sustain. Energy Rev.* 119 (2020), <https://doi.org/10.1016/j.rser.2019.109600>.
- [47] D. López-Díaz, M. López Holgado, J.L. García-Fierro, M.M. Velázquez, Evolution of the Raman spectrum with the chemical composition of graphene oxide, *J. Phys. Chem. C* 121 (2017) 20489–20497, <https://doi.org/10.1021/acs.jpcc.7b06236>.
- [48] A.A.K. King, B.R. Davies, N. Noorbehesht, P. Newman, T.L. Church, A.T. Harris, J. M. Razal, A.I. Minett, A new raman metric for the characterisation of graphene oxide and its derivatives, *Sci. Rep.* 6 (1) (2016) 6, <https://doi.org/10.1038/srep19491>.
- [49] A.Y. Lee, K. Yang, N.D. Anh, C. Park, S.M. Lee, T.G. Lee, M.S. Jeong, Raman study of D* band in graphene oxide and its correlation with reduction, *Appl. Surf. Sci.* 536 (2021) 147990, <https://doi.org/10.1016/j.apsusc.2020.147990>.
- [50] D. Gabriëls, W.Y. Hernández, B.F. Sels, P. Van Der Voort, A. Verberckmoes, Review of catalytic systems and thermodynamics for the Guerbet condensation reaction and challenges for biomass valorization, *Catal. Sci. Technol.* 5 (2015) 3876–3902, <https://doi.org/10.1039/c5cy00359h>.
- [51] Y. Tong, J.H. Lunsford, Mechanistic and kinetic studies of the reactions of gas-phase methyl radicals with metal oxides, *J. Am. Chem. Soc.* 113 (1991) 4741–4746, <https://doi.org/10.1021/ja00013a005>.
- [52] M. Anpo, G. Costentin, E. Giamello, H. Lauron-Pernot, Z. Sojka, Characterisation and reactivity of oxygen species at the surface of metal oxides, *J. Catal.* 393 (2021) 259–280, <https://doi.org/10.1016/j.jcat.2020.10.011>.
- [53] LiMgO, *Nature* 1985, *Nature*. 314 (1985) 721.
- [54] H. Xu, H. Li, Alcohol-assisted hydrodeoxygenation as a sustainable and cost-effective pathway for biomass derivatives upgrading, *J. Energy Chem.* 73 (2022) 133–159, <https://doi.org/10.1016/j.jechem.2022.05.021>.